JOURNAL OF SYNCHROTRON RADIATION
ISSN 1600-5775

Local structure investigation of Co–Fe–Si–B ribbons by extended X-ray absorption fine-structure spectroscopy

A. A. Deshmukh,[a,b]* A. P. Srivastava,[c] J. P. Singh,[d] Manish Kumar,[d] K. H. Chae,[e] K. Asokan[f] and U. A. Palikundwar[a]*

[a]X-ray Research Laboratory, Department of Physics, Rashtrasant Tukadoji Maharaj Nagpur University, Nagpur, MS 440033, India, [b]Department of Metallurgical and Materials Engineering, National Institute of Technology, Rourkela, Odisha 769008, India, [c]Mechanical Metallurgy Division, Bhabha Atomic Research Centre, Mumbai, MS 400085, India, [d]Pohang Accelerator Laboratory, Pohang University of Science and Technology, Pohang 37673, Republic of Korea, [e]Advanced Analysis Center, Korea Institute of Science and Technology, Seoul 2792, Republic of Korea, and [f]Inter-University Accelerator Centre (IUAC), Aruna Asaf Ali Marg, New Delhi 110 067, India. *Correspondence e-mail: akdeshmukh9@gmail.com, uapali@yahoo.com

Received 22 July 2020
Accepted 13 November 2020

Edited by G. Grübel, HASYLAB at DESY, Germany

Keywords: Co-rich glassy ribbons; EXAFS; coordination number; thermodynamic parameter.

Supporting information: this article has supporting information at journals.iucr.org/s

In the present work, extended X-ray absorption fine-structure (EXAFS) investigations of $Co_{69}Fe_xSi_{21-x}B_{10}$ (x = 3, 5, 7) glassy ribbons were performed at the Co K-edge. The magnitude of the first peak of the Fourier transforms of the EXAFS signals is found to increase monotonically with increasing Si concentrations indicating the formation of the localized ordered structure at the atomic scale. The Co–Si coordination number (CN) increases at the expense of the CN of Co/Fe. Smaller interatomic distances are observed in the glassy phase compared with that in the crystalline phase which promotes the stability of the glassy phase. Calculations of the thermodynamic parameter (P_{HSS}), cohesive energy (E_C) and the atomic radius difference (δ) parameter show that the alloy composition $Co_{69}Fe_3Si_{18}B_{10}$ has a good glass-forming ability (GFA) with the highest CN of Si compared with other compositions. A linear correlation of CN with that of the GFA parameter (P_{HSS}) exists and the CN also plays a crucial role in the GFA of the glassy alloys. This parameter should be considered in developing different GFA criteria.

1. Introduction

Cobalt (Co) based glassy alloys were found to have low magnetostriction and low coercivity, high initial and maximal permeability (Babilas *et al.*, 2012; Vojtanik, 2006; Zakharenko *et al.*, 2006; Bednarcik *et al.*, 2004). These glassy alloys have applications in various fields which include magnetic wires, magnetic sensors, band-pass filters and magnetic shielding (Babilas *et al.*, 2012; Vojtanik, 2006; Zakharenko *et al.*, 2006; Bednarcik *et al.*, 2004). Earlier, numerous Co-based ternary alloys such as Co–Si–B (Kulik *et al.*, 1984; Hagiwara *et al.*, 1982; Baczewski *et al.*, 1984; Barquin *et al.*, 1994; Inoue *et al.*, 1995; Wexler & Emr, 1997; Wang *et al.*, 2007), Co–Ta–B (Yu *et al.*, 2014), quaternary alloys such as Co–Fe–Si–B (Babilas *et al.*, 2012; Bednarcik *et al.*, 2004; Kulik *et al.*, 1984; Liu *et al.*, 2012; Janotová *et al.*, 2014; Srivastava *et al.*, 2016), Co–Fe–B–Nb (Gupta *et al.*, 2012), Co–Fe–Ta–B (Taghvaei & Eckert, 2016), quinary alloys such as Co–Fe–Si–B–Nb (Janotová *et al.*, 2014; Sidorov *et al.*, 2014; Man *et al.*, 2010; Dong *et al.*, 2012; Liao *et al.*, 2019), Co–Fe–Si–B–Ni (Srivastava *et al.*, 2012) and hexenary alloys such as Co–Fe–Si–B–Nb–Ga (Hosko *et al.*, 2012) were investigated for different magnetic and mechanical properties. Nevertheless, the glass-forming ability (GFA) of Co-based bulk metallic glasses (BMGs) was found to be

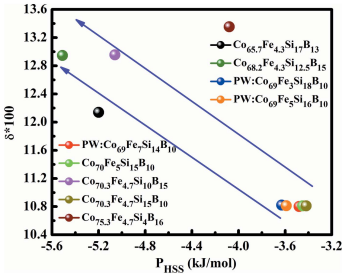

inferior in comparison with Pd, Zr and Cu-based BMGs (Wang *et al.*, 2007) because of the requirement of the higher cooling rate of about 10^5 K s^{-1} (Shen *et al.*, 2007) to form a glassy alloy. This results in smaller sample thickness, limited to 50 µm or less in Co–Si–B alloy (Shen *et al.*, 2007) achieved by the melt spinning method, and 1 to 6 mm in diameter for Co–Fe–Si–B–Nb alloy achieved by copper mould casting method (Sidorov *et al.*, 2014; Man *et al.*, 2010; Dong *et al.*, 2012). However, very little attention has been given to understanding the local structure influencing the thermal stability and GFA of the Co-based alloys.

On the other hand, there are different experimental techniques such as X-ray scattering (Matsubara *et al.*, 1989; Antonowicz, 2010; Saporiti *et al.*, 2010), neutron diffraction (Hsieh *et al.*, 1990), electron diffraction (Li *et al.*, 2009) and extended X-ray absorption fine-structure (EXAFS) spectroscopy (Saksl *et al.*, 2005; Zalewski *et al.*, 2009) which are very useful to study the glassy phase and the local atomic structure in metallic glasses (MGs). Among them, EXAFS is element-selective and probes the local environment such as coordination numbers (CNs), bond distances (R), and their distribution around the absorbing atomic species such as transition metal (TE) and rare earth (RE) (Xiong *et al.*, 2019; Dziegielewski *et al.*, 2020). Earlier, EXAFS investigations were performed for different families of MGs such as Al-based (Li *et al.*, 2009; Saksl *et al.*, 2005; Zalewski *et al.*, 2009; Xiong *et al.*, 2019), Cu–Zr (Dziegielewski *et al.*, 2020), Co-based (Fdez-Gubieda *et al.*, 1992; Fdez-Gubieda *et al.*, 1995), Pd-based (Kumar *et al.*, 2011) and Ti-based (Kim *et al.*, 2007) MGs to investigate the local order influence of glass formation. This has motivated us to evaluate the glass formation ability in $Co_{69}Fe_xSi_{21-x}B_{10}$ (x = 3, 5, 7) glassy ribbons in terms of the local structure around Co by investigating EXAFS associated with the Co K-edge.

2. Experimental details

In an earlier report (Srivastava *et al.*, 2016), complete details about the synthesis of $Co_{69}Fe_xSi_{21-x}B_{10}$ (x = 3, 5, 7) glassy ribbons have been presented. Compositions $Co_{69}Fe_3Si_{18}B_{10}$, $Co_{69}Fe_5Si_{16}B_{10}$ and $Co_{69}Fe_7Si_{14}B_{10}$, hereafter referred to as SA, SB and SC, respectively. X-ray absorption spectroscopy experiments at the Co K-edge were performed at beamline 7D XAFS, PL-II synchrotron source, Pohang Accelerator Laboratory (Pohang, South Korea) in fluorescent mode at room temperature using a Si(111) double-crystal monochromator. The energy resolution ($\Delta E/E$) of the monochromator is approximately 2×10^{-5} in the energy range studied in the present work. Due to the higher thickness of the ribbon (20 µm), the simultaneous measurement of standard Co foil was not possible. Therefore, Co foil was measured before measuring the actual samples. The absorption coefficient has been determined by using an ionization chamber, filled with a nitrogen (N) and argon (Ar) gas mixture, to record the flux intensity before the sample (I_0), and a passivated implanted planar silicon (PIPS) detector was used to record fluorescence intensity (I_F). Two absorption scans were collected for each sample at the Co K-edge to ensure the consistency of the spectra. The energies of absorption K-edges corresponding to Si (1839 eV) and B (188 eV) lie below the energy range (4–21 keV) of beamline 7D XAFS of the PL-II synchrotron source. On the other hand, a small at.% of Fe discouraged considering the Fe K-edge in the present investigation. Therefore, the EXAFS associated with these edges have not been considered. The orthorhombic crystallographic information of $Fe_3Si_{0.4}B_{0.6}$ glassy alloy (Wirginia & Jacek, 2013) was considered for fitting the EXAFS data.

Table 1
Orthorhombic model of $Fe_3Si_{0.4}B_{0.6}$ glassy alloy (Wirginia & Jacek, 2013).

Final orthorhombic model (*Pnma*) (62):	a = 4.845 Å, b = 7.058 Å, c = 4.4370 Å		
Atoms	x	y	z
Co/Fe	0.2116	0.0675	0.6180
Si	0.0287	0.25	0.6180
B	0.4578	0.25	0.5782

3. Data analysis

In the present work, EXAFS spectra have been processed and analysed using the *IFEFFIT* version 1.2.9 software package (Ravel & Newville, 2005). The energy calibration was carried out for the Co K-edge by assigning an energy equal to 7709 eV to the first inflection point of the main edge in Co metal foil. Further, the spectrum of all the samples on the same scale was aligned and the maxima of the first derivative of the experimentally measured absorption coefficient $\mu(E)$ was considered as the threshold energy (E_0) for all the measurements. The EXAFS function $\chi(k)$ was obtained by subtracting a linear function obtained by fitting the pre-edge region (−200 eV to −50 eV concerning the edge) from the entire raw spectra and free atom background simulated by fitting a cubic spline function to the post-edge region (50–1000 eV beyond the edge). The standard software package *Athena/Artemis* (Ravel & Newville, 2005) was used to transform the measured EXAFS spectra into k-space (3.0–10.0 $Å^{-1}$). In this, it is assumed that there is no difference between Co and Fe ions as backscatters because of their very similar atomic number. Further, data have been fitted using the crystallographic information of the $Fe_3Si_{0.4}B_{0.6}$ alloys (Table 1) from an earlier report (Wirginia & Jacek, 2013). The software (Ravel & Newville, 2005) computes the theoretical spectrum from the given model using the *ATOM* and *FEFF6* subroutines (Rehr & Albers, 2000; Rehr *et al.*, 2009). Information on the coordination number (CN), interatomic distances (R) and mean squared relative displacement of the effective interatomic distances (σ^2) have been extracted using a single-shell model. The amplitude reduction factor (s_0^2) was set to 0.23 for all the samples. The fitting was performed for the first peak in Fourier-filtered R space with the fittings range 1.05–2.915 Å. The number of independent points according to the Nyquist criterion was always greater than 6 for all the samples. The spatial resolution defined as $\Delta R = \pi/2(k_{max} - k_{min})$ (Stern *et al.*, 1995) for the present measurement was found to be

Table 2
Coordination number (CN), interatomic distances (R) and mean squared relative displacement of the effective interatomic distances (σ^2) of the EXAFS analysis for Co–Fe–Si–B glassy ribbons at the Co K-edge.

Compositions	CN			R (Å)						σ^2		
	Co–Co/Fe	Co–Si	Co–B	Co–Co/Fe		Co–Si		Co–B		Co–Co/Fe	Co–Si	Co–B
				R_{eff}	R_{fit}	R_{eff}	R_{fit}	R_{eff}	R_{fit}			
$Co_{69}Fe_7Si_{14}B_{10}$	9.28 (0.02)	4.00 (0.02)	4.00 (0.02)	2.443	2.466 (0.023)	1.563	1.633 (0.070)	1.764	1.683 (0.080)	0.011 (0.003)	0.029 (0.007)	(0.010) (0.004)
$Co_{69}Fe_5Si_{16}B_{10}$	9.24 (0.02)	4.04 (0.02)	4.00 (0.02)	2.443	2.454 (0.011)	1.563	1.708 (0.145)	1.764	1.762 (0.001)	0.011 (0.008)	0.035 (0.019)	0.013 (0.013)
$Co_{69}Fe_3Si_{18}B_{10}$	9.20 (0.02)	4.08 (0.02)	4.00 (0.02)	2.443	2.470 (0.027)	1.563	1.666 (0.102)	1.764	1.711 (0.053)	0.011 (0.005)	0.024 (0.008)	0.007 (0.006)

$\sim$0.22 Å. The complete processing and analysis procedures of the data are described in the following steps.

Step 1. Firstly, data of the sample SA ($Co_{69}Fe_3Si_{18}B_{10}$) was processed using *Athena* software (Ravel & Newville, 2005) by setting the k-range to 3.5–10 Å^{-1} and the R range to 1.4−2.78 Å with an Rbkg value of 1.7. Further, self-absorption correction to the data was performed using the Booth function. The sample thickness (20 µm) and the composition formula for sample SA, *i.e.* $Co_{69}Fe_3Si_{18}B_{10}$, were given as input parameters. It was observed that the Rbkg value sets back to 1.0 and becomes frozen with all other parameters except the k and R range values. A similar procedure was followed for other samples: SB ($Co_{69}Fe_5Si_{16}B_{10}$) and SC ($Co_{69}Fe_7Si_{14}B_{10}$), respectively. After processing all the samples, data were saved for further analysis using *Artemis* software (Ravel & Newville, 2005).

Step 2. Data of sample SA were imported to the *Artemis* (Ravel & Newville, 2005). Further, the crystallographic information of $Fe_3Si_{0.4}B_{0.6}$ (Wirginia & Jacek, 2013) was provided for the fitting of the data. A single scattering path such as Co–Co/Fe, Co–Si, Co–B was considered for the analysis. The default values of the coordination number (CN) for the Co–Co/Fe, Co–Si, Co–B pair are 2, 1, and 1, respectively.

Step 3. Amplitude reduction parameter (s_0^2), enot (ΔE_0), interatomic distance (R) and mean squared relative displacement of the effective interatomic distances (σ^2) were set as 'guess' parameter initially with $s_0^2 = 1$, $\Delta E_0 = 0$, $\Delta R = 0$ and $\sigma^2 = 0.003$. Earlier (Fdez-Gubieda *et al.*, 1992), it was reported that Co-based metallic glasses give the CN in the range 7–11 at the Co K-edge.

Step 3.1. Initially CN of Co was set to 7 and that of Si and B to 1 and fitting was performed. Further, CN of Co was varied from 7 to 11 in steps of 1 with constant CN of Si and B. The k-range was set to 3.0–10.0 Å^{-1} and the R range to 1.05–2.915 Å. The observations for the best fit were noted.

Step 3.2. CN of Si was increased to 2 by keeping CN of B at a constant value of 1. Again CN of Co was varied from 7 to 11. CN of Si was varied from 1 to 4. The k and R range was fixed as in Step 3.1. The observations for the best fit were noted.

Step 3.3. CN of B was increased to 2 and CN of Si was kept constant at 1. Again CN of Co was varied from 7 to 11. CN of B was varied from 1 to 4. The k and R range was fixed as in Step 3.1. The observations for the best fit were noted.

From Step 3.1 to Step 3.3 only one CN was allowed to vary at a time so that the effect of that particular CN could be analyzed on the data. Fitting parameters such as s_0^2, ΔE_0, ΔR, and σ^2 were allowed to vary during each fitting. The best fit for sample SA was obtained at $s_0^2 = 0.230$.

Step 4: Step 3.1 to Step 3.3 has been used for the sample SB ($Co_{69}Fe_5Si_{16}B_{10}$) and sample SC ($Co_{69}Fe_7Si_{14}B_{10}$), respectively, with $s_0^2 = 0.230$ (fixed). Further, all the fitting parameters obtained are given in Table 2.

4. Results and discussion

The Fourier transforms (FTs) of the EXAFS signals weighted by k^3 for SA, SB and SC samples at the Co K-edge are shown in Figs. 1(*a*), 1(*b*) and 1(*c*), respectively, with the corresponding fits. A similar qualitative appearance exists in all of these three samples in the figures. From these figures, it is evident that one peak exhibits near $R = 2$ Å for samples SA, SB and SC whereas beyond $R = 2.9$ Å there is no appreciable change in the structural features. This indicates the lack of long-range order around Co in all these samples. These observations are identical to that of Fe–Co–Si–B as reported by Fdez-Gubieda *et al.* (1992). It can be seen that with an increase in Si concentration there is a corresponding increase in the magnitude of the peak for SA, SB and SC. A very small change in the peak position of all the three samples has been observed with decreasing Si concentration. From Table 2, it can be observed that with a decrease in Si concentration there is a corresponding decrease in CN around the Co atom. The CN of B remains constant around the Co atom. Interatomic distances between the Co and Co/Fe atom are small compared with that of the Goldsmith radii [$R_{Co–Co} = 2.502$ Å, $R_{Co–Fe} = 2.482$ Å (Dolan *et al.*, 2006)]. Similarly, interatomic distances between Co and Si/B atoms are small compared with their atomic radii [$R_{Co–Si} = 2.404$ Å, $R_{Co–B} = 2.071$ Å (Dolan *et al.*, 2006)]. The formation of the stable glassy phase can be presumed if the first neighbour distances are smaller compared with that of the crystalline distances as it enables the atoms to occupy the position in the short-range order (SRO) region (Galván-Colín *et al.*, 2015). This supports the formation of the stable glassy phase in the present quaternary Co–Fe–Si–B glassy ribbons. For the Co–Co/Fe pair, the interatomic distance (R) is found to decrease from 2.466 Å to 2.454 Å with increasing Co–Si CN from 4.0 to 4.04. This is

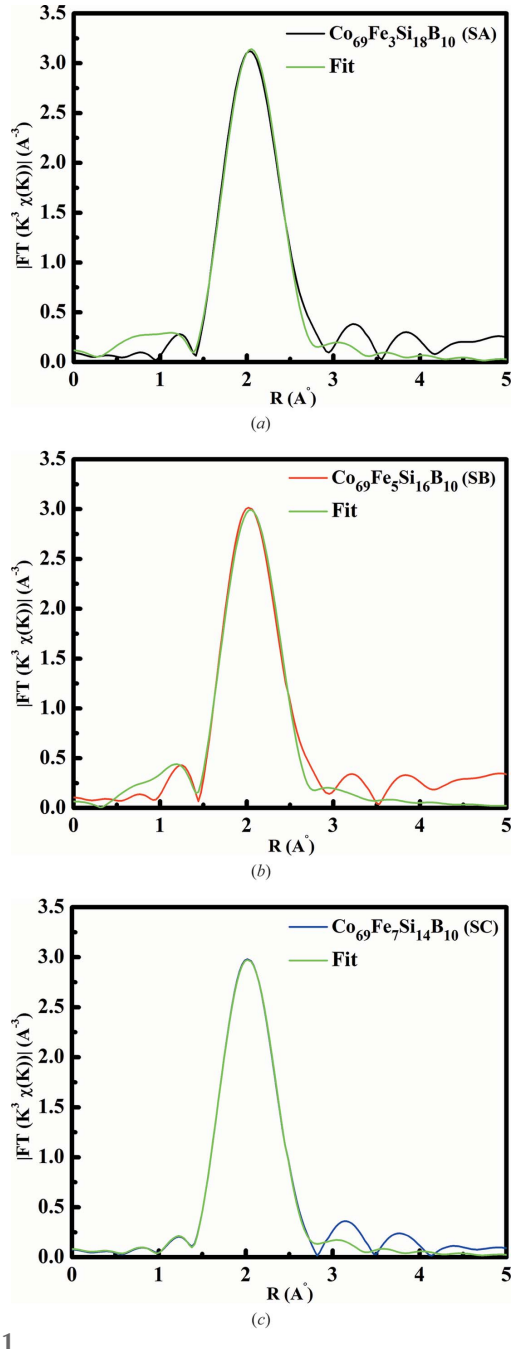

Figure 1
Fourier transforms of EXAFS oscillations in R space for (*a*) SA, (*b*) SB and (*c*) SC at the Co K-edge.

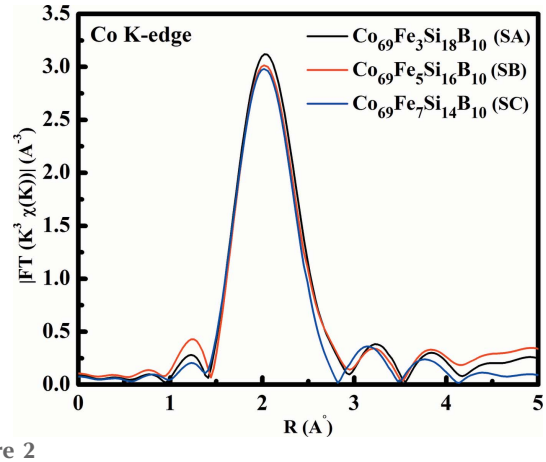

Figure 2
Fourier transforms of EXAFS oscillations in R space for SA, SB and SC at the Co K-edge.

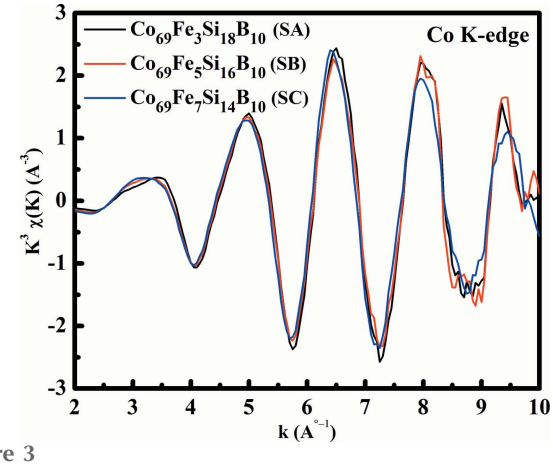

Figure 3
k^3-Weighted EXAFS oscillations for SA, SB and SC at the Co K-edge.

followed by a further increase in R to 2.470 Å with an increase in CN from 4.04 to 4.08. On the other hand, for the Co–Si pair, R first increases from 1.633 Å to 1.708 Å with an increase in CN of Si from 4.0 to 4.04 and then decreases from 1.708 Å to 1.667 Å with an increase of CN of Si from 4.04 to 4.08. A similar trend has also been observed for Co–B pairs. Fig. 2 shows the FT of EXAFS oscillations in R space and Fig. 3 shows k^3-weighted EXAFS oscillations for SA, SB and SC at the Co K-edge. From Fig. 2, it can be seen that with increasing Si concentration the magnitude of the first peak corresponding to nearest neighbours around Co increases indicating the formation of the stable glassy phase with the favourable ordered structure at the atomic scale. In order to rationalize these findings, thermodynamic and topological parameters such as enthalpy of mixing ($\Delta H_{\rm alloy}^{\rm mix}$), atomic size difference resulting in mismatch entropy ($\Delta S_\sigma/k_{\rm B}$) and atomic arrangements leading to configurational entropy ($\Delta S_{\rm C}/R$) and $P_{\rm HSS}$ were calculated. Details of these parameters are given in the supporting information. Earlier, Chattopadhyay *et al.* (2016) reported that for Co-based glasses $\Delta H_{\rm alloy}^{\rm mix}$ ranges from −30 to −10 kJ mol^{-1} and the $\Delta S_\sigma/k_{\rm B}$ range is in a wide window of 0.2–0.8. In the present work, the values of $\Delta H_{\rm alloy}^{\rm mix}$ (−17.19 to −18.72 kJ mol^{-1}) and $\Delta S_\sigma/k_{\rm B}$ (0.213 to 0.215) falls within the above range. Further, a correlation between CN of Si and $P_{\rm HSS}$ is illustrated in Fig. 4. This figure shows that, with a decrease in Si concentration, $P_{\rm HSS}$ of the alloy becomes more positive (*i.e.* less negative). Ramakrishna Rao *et al.* (2013) have successfully used the $P_{\rm HSS}$ parameter for Fe-based MG where they reported that the model incorporating $\Delta H_{\rm alloy}^{\rm mix}$, $\Delta S_\sigma/k_{\rm B}$, $\Delta S_{\rm c}/R$ are more effective in the selection of the compositions in multicomponent systems with good GFA (Ramakrishna Rao *et al.*, 2013). They showed that a large negative $\Delta H_{\rm alloy}^{\rm mix}$ may favour the glass formation. Besides, a large atomic size

Table 3
Thermodynamic (ΔH_{alloy}^{mix}), topological (S_σ/k_B, S_C/R) parameters, cohesive energy (E_C), atomic radius difference ($\delta \times 100$) of Co–Fe–Si–B glassy ribbon.

Composition	ΔH_{alloy}^{mix} (kJ mol^{-1})	S_σ/k_B	S_C/R	E_C (kJ mol^{-1})	$\delta \times 100$	Reference	P_{HSS} (kJ mol^{-1})
$Co_{65.7}Fe_{4.3}Si_{17}B_{13}$	−19.63	0.271	0.978	442.11	12.138	Hagiwara *et al.* (1982)	−5.20
$Co_{68.2}Fe_{4.3}Si_{12.5}B_{15}$	−19.07	0.307	0.941	446.83	12.947	Liao *et al.* (2019)	−5.51
$Co_{69}Fe_3Si_{18}B_{10}$	−18.72	0.215	0.900	441.33	10.821	Present work	−3.63
$Co_{69}Fe_5Si_{16}B_{10}$	−17.98	0.214	0.929	440.67	10.813	Present work	−3.59
$Co_{69}Fe_7Si_{14}B_{10}$	−17.19	0.213	0.947	440.01	10.802	Present work	−3.48
$Co_{70}Fe_5Si_{15}B_{10}$	−17.61	0.214	0.914	440.45	10.810	Hagiwara *et al.* (1982)	−3.45
$Co_{70.3}Fe_{4.7}Si_{10}B_{15}$	−18.18	0.307	0.906	446.23	12.956	Inoue *et al.* (1995)	−5.06
$Co_{70.3}Fe_{4.7}Si_{15}B_{10}$	−17.61	0.214	0.906	440.48	10.811	Hagiwara *et al.* (1982)	−3.42
$Co_{75.3}Fe_{4.7}Si_4B_{16}$	−16.15	0.324	0.779	446.28	13.354	Hagiwara *et al.* (1982)	−4.08

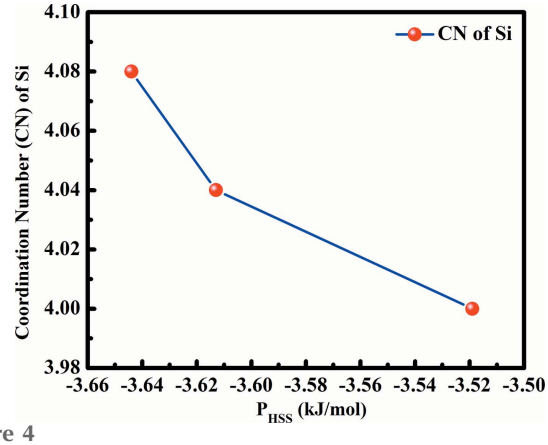

Figure 4
Variation in coordination number (CN) of Si with P_{HSS}.

difference may allow the smallest of the species to occupy interstitial positions without inducing much strain in the lattice, resulting in glass formation with higher GFA (Ramakrishna Rao *et al.*, 2013). The multiplication of ΔH_{alloy}^{mix}, $\Delta S_\sigma/k_B$, $\Delta S_c/R$ has been performed to acquire the most negative value of P_{HSS} thereby increasing the GFA. This helped to increase the viscosity of the alloy and restricts the atomic mobility thereby having efficient atomic packing (Ramakrishna Rao *et al.*, 2013). Restricted atomic mobilities help to suppress the nucleation which stabilizes the liquid at low temperatures and thereby it turn into a glass upon cooling (Ramakrishna Rao *et al.*, 2013). Fig. 4 shows the variation of CN of Si with that of P_{HSS}. This suggests that a higher negative value of P_{HSS}, which is indicative of a higher GFA of the alloy, is related to the increase in the CN of Si. Additionally, the cohesive energy (E_C) of the Co–Fe–Si–B alloy has also been calculated in the present investigation and compared with that of other Co-based MGs from the literature and illustrated in Fig. 5. From this figure and Table 3, it can be seen that E_C increases as P_{HSS} becomes more negative. This trend is also followed by other Co-based MGs which compliment the present observations. Therefore, the increase in CN of Si can be correlated to an increase in E_C and this may be attributed to the covalent bonding nature of the Si. In the present work, SA has the most negative P_{HSS} (−3.63 kJ mol^{-1}) and highest cohesive energy (441.33 kJ mol^{-1}). On the other hand, SC has a less negative P_{HSS} (−3.48 kJ mol^{-1}) and smallest cohesive energy (440.01 kJ mol^{-1}). Further, to understand the P_{HSS} dependence of Si, the correlation between the atomic radius difference parameter (δ) and that of P_{HSS} has also been evaluated. Details of the δ parameter are given in the supporting information. Fig. 6 shows the variation in δ and P_{HSS}. A similar trend as observed with E_C can be noticed for δ and P_{HSS} for different Co–Fe–Si–B glass-forming compositions. It has been reported earlier that the large atomic mismatch increases the free energy in an alloy and lowers the stability of the solid solution thereby promoting the glassy phase formation in the alloy (Zhang *et al.*, 2008; Guo & Liu,

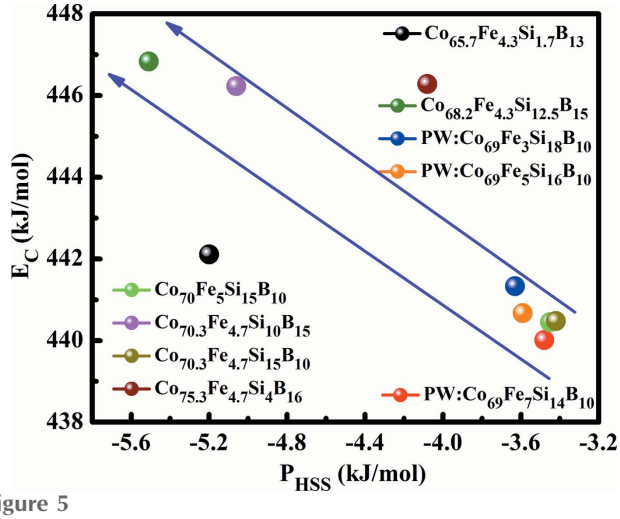

Figure 5
Variation in cohesive energy (E_C) with P_{HSS}.

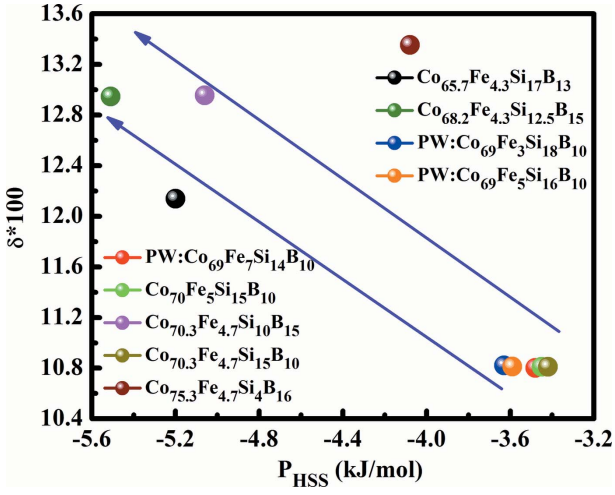

Figure 6
Atomic radius mismatch (δ) with P_{HSS}.

2011). Besides, a local elastic strain is produced due to the atomic differences (Guo & Liu, 2011). The numerical value $\delta \geq 9$ supports the glassy phase formation in the liquid melt after quenching. In the present work, a value of $\delta > 10$ suggests the initiation of atomic stress and an increase in free energy with an increase in CN of Si around the Co atom. This endorses the observation of an increase in GFA with increased Si concentration in the present quaternary Co–Fe–Si–B glassy ribbons. Therefore, it is presumed that the addition of Si to Co–Fe–B is significant and the Co–Si CN plays an important role in enhancing the GFA of the alloy.

5. Conclusions

According to the EXAFS fitted data, the local structure of Co is found to be concentration-dependent. The nearest-neighbour CN of Si around the Co atom increases at the expense of the Co/Fe CN with an increase in Si concentrations in the alloy composition. It is also noticed that $Co_{69}Fe_3Si_{18}B_{10}$ (SA) has the best glass-forming ability with the highest CN of Si compared with other compositions. The interatomic distances between the Co and Fe/Si/B atoms are small compared with their atomic radii thereby promoting the atoms to occupy the position in the SRO regime in Co–Fe–Si–B alloy. A linear correlation of CN of Si around the Co atom with the GFA parameter P_{HSS} shows that the CN also plays an important role in the GFA of the glassy alloys. Additionally, an increase in cohesive energy and atomic radius mismatch with an increase in CN is found to significantly contribute to the good glass-forming ability in SA. Therefore, while developing different GFA criteria, CN should be considered.

6. Related literature

The following references, not cited in the main body of the paper, have been cited in the supporting information: Bhatt *et al.* (2007); Gallego *et al.* (1990); Khond *et al.* (2018).

Acknowledgements

The authors are thankful to the Pohang Accelerator Laboratory, Pohang, South Korea, to carry out the synchrotron XRD and EXAFS measurements.

Funding information

The following funding is acknowledged: University Grants Commission [(UGC, New Delhi, India, scholarship to AAD, Basic Science Research (BSR) fellowship to carry out this research work].

References

Antonowicz, J. (2010). *J. Mater. Sci.* **45**, 5040–5044.
Babilas, R., Nowosielski, R., Dercz, G., Stokłosa, Z. & Głuchowski, W. (2012). *Arch. Mater. Sci. Eng.* **54**, 37–44.
Baczewski, L. T., Kaczkowski, Z. & Lipiński, E. (1984). *J. Magn. Magn. Mater.* **41**, 346–348.
Barquin, L. F., Gomez Sal, J. C., Barandiarin, J. M., Bermejo, F. J. & Howells, W. S. (1994). *J. Phys. Condens. Matter*, **6**, 164–1652.
Bednarčík, J., Kováč, J., Kollár, P., Roth, S., Sovák, P., Balcerski, J., Polanski, K. & Švec, T. (2004). *J. Non-Cryst. Solids*, **337**, 42–47.
Bhatt, J., Jiang, W., Junhai, X., Qing, W., Dong, C. & Murty, B. S. (2007). *Intermetallics*, **15**, 716–721.
Chattopadhyay, C., Satish Idury, K. S. N., Bhatt, J., Mondal, K. & Murty, B. S. (2016). *Mater. Sci. Technol.* **32**, 380–400.
Dolan, M. D., Dave, N. C., Ilyushechkin, A. Y., Morpeth, L. D. & McLennan, K. G. (2006). *J. Membr. Sci.* **285**, 30–55.
Dong, Y., Wang, A., Man, Q. & Shen, B. (2012). *Intermetallics*, **23**, 63–67.
Dziegielewski, P., Mathon, O., Kantor, I., Pascarelli, S., Shinmei, T., Irifune, T. & Antonowicz, J. (2020). *High. Press. Res.* **40**, 54–64.
Fdez-Gubieda, M. L., Barandiarán, J. M., Plazaola, F., Hernando, A. & Mobilio, S. (1992). *J. Non-Cryst. Solids*, **151**, 51–58.
Fdez-Gubieda, M. L., Orue, I., Plazaola, F. & Barandiarán, J. M. (1995). *Physica B*, **208–209**, 365–366.
Gallego, L. J., Somoza, J. A. & Alonso, J. A. (1990). *J. Phys. Condens. Matter*, **2**, 6245–6250.
Galván-Colín, J., Valladares, A. A., Valladares, R. M. & Valladares, A. (2015). *Physica B*, **475**, 140–147.
Guo, S. & Liu, C. T. (2011). *Prog. Nat. Sci.: Mater. Int.* **21**, 433–446.
Gupta, P., Ganguli, T., Gupta, A., Sinha, A. K., Deb, S. K., Svec, P. Jr & Franco, V. (2012). *J. Appl. Phys.* **111**, 113518.
Hagiwara, M., Inoue, A. & Masumoto, T. (1982). *Mater. Sci. Eng.* **54**, 197–207.
Hosko, J., Janotova, I., Svec, P., Janickovic, D., Vlasak, G., Illekova, E., Matko, I., Svec, P. Sr (2012). *J. Non-Cryst. Solids*, **358**, 1545–1549.
Hsieh, H. Y., Toby, B. H., Egami, T., He, Y., Poon, S. J. & Shiflet, G. J. (1990). *J. Mater. Res.* **5**, 2807–2812.
Inoue, A., Katsuya, A., Amiya, K. & Masumoto, T. (1995). *Met. Trans. JIM*, **36**, 802–809.
Janotová, I., Švec, P., Mater'ko, I., Janičkovič, D., Švec, P. Sr (2014). *J. Alloys Compd.* **615**, S198–S202.
Khond, A., Babu, D. A., Smaran, S., Deshmukh, A., Majumdar, B., Bhatt, J. & Srivastav, A. K. (2018). *J. Non-Cryst. Solids*, **500**, 191–195.
Kim, Y. C., Chang, H. J., Kim, D. H., Kim, W. T. & Cha, P. R. (2007). *J. Phys. Condens. Matter*, **19**, 196104.
Kulik, T., Matyja, H. & Lisowski, B. (1984). *J. Magn. Magn. Mater.* **43**, 135–142.
Kumar, V., Fujita, T., Konno, K., Matsuura, M., Chen, M. W., Inoue, A. & Kawazoe, Y. (2011). *Phys. Rev. B*, **84**, 134204.
Li, G., Borisenko, K. B., Chen, Y., Nguyenmanh, D., Ma, E. & Cockayne, D. J. H. (2009). *Acta Mater.* **57**, 804–811.
Liao, W. B., Jiang, C., Xu, S., Gao, L., Zhang, H., Li, P., Liu, Z. & Lu, Y. (2019). *Mater. Res. Expr.* **6**, 106565.
Liu, J. S., Cao, F. Y., Xing, D. W., Zhang, L. Y., Qin, F. X., Peng, H. X., Xue, X. & Sun, J. F. (2012). *J. Alloys Compd.* **541**, 215–221.
Man, Q., Sun, H., Dong, Y., Shen, B., Kimura, H., Makino, A. & Inoue, A. (2010). *Intermetallics*, **18**, 1876–1879.
Matsubara, E., Waseda, Y., Inoue, A. & Masumoto, T. (1989). *Z. Naturforsch.* **44**, 814–820.
Ramakrishna Rao, B., Srinivas, M., Shah, A. K., Gandhi, A. S. & Murty, B. S. (2013). *Intermetallics*, **35**, 73–81.
Ravel, B. & Newville, M. (2005). *J. Synchrotron Rad.* **12**, 537–541.
Rehr, J. J. & Albers, R. C. (2000). *Rev. Mod. Phys.* **72**, 621–654.
Rehr, J. J., Kas, J. J., Prange, M. P., Sorini, A. P., Takimoto, Y. & Vila, F. (2009). *C. R. Phys.* **10**, 548–559.
Saksl, K., Jóvári, P., Franz, H. & Jiang, J. Z. (2005). *J. Appl. Phys.* **97**, 113507.
Saporiti, F., Boudard, M. & Audebert, F. (2010). *J. Alloys Compd.* **495**, 309–312.
Shen, B., Koshiba, H., Inoue, A., Kimura, H. & Mizushima, T. (2007). *Mater. Sci. Forum*, **42**, 2136–2139.

Sidorov, V., Hosko, J., Mikhailov, V., Rozkov, I., Uporova, N., Svec, P., Janickovic, D., Matko, I., Svec Sr, P. & Malyshev, L. (2014). *J. Magn. Magn. Mater.* **354**, 35–38.
Srivastava, A. P., Das, N., Sharma, S. K., Sinha, A. K., Srivastava, D., Pujari, P. K. & Dey, G. K. (2016). *J. Phys. D Appl. Phys.* **49**, 225303.
Srivastava, A. P., Srivastava, D., Sudarshan, K., Sharma, S. K., Pujari, P. K., Majumdar, B., Suresh, K. G. & Dey, G. K. (2012). *J. Magn. Magn. Mater.* **324**, 2476–2482.
Stern, E. A., Newville, M., Ravel, B., Yacoby, Y. & Haskel, D. (1995). *Physica B*, **208–209**, 117–120.
Taghvaei, A. H. & Eckert, J. (2016). *J. Alloys Compd.* **675**, 223–230.
Vojtanik, P. (2006). *J. Magn. Magn. Mater.* **304**, 159–163.
Wang, Q., Zhu, C., Li, Y., Wu, J., Dong, C., Qiang, J., Zhang, W. & Inoue, A. (2007). *Mater. Sci. Forum*, **561–565**, 1275–1278.
Wexler, D. & Emr, M. (1997). *Mater. Sci. Eng. A*, **226–228**, 1064–1068.
Wirginia, P. & Jacek, P. (2013). *Solid State Phenom.* **203–204**, 386–389.
Xiong, X. Z., Yi, J. J., Kong, L. T., Jiang, Z., Huang, Y. Y. & Li, J. F. (2019). *Intermetallics*, **111**, 106505.
Yu, P. F., Feng, S. D., Xu, G. S., Guo, X. L., Wang, Y. Y., Zhao, W., Qi, L., Li, G., Liaw, P. K. & Liu, R. P. (2014). *Scr. Mater.* **90–91**, 45–48.
Zakharenko, M., Babich, M., Yeremenko, G. & Semen'ko, M. (2006). *J. Magn. Magn. Mater.* **304**, e525–e527.
Zalewski, W., Antonowicz, J., Bacewicz, R. & Latuch, J. (2009). *J. Alloys Compd.* **468**, 40–46.
Zhang, Y., Zhou, Y. J., Lin, J. P., Chen, G. L. & Liaw, P. K. (2008). *Adv. Eng. Mater.* **10**, 534–538.